

Orbital angular momentum conversion of acoustic vortex beams via planar lattice coupling

Qingbang Han(韩庆邦), Zhipeng Liu(刘志鹏), Cheng Yin(殷澄), Simeng Wu(吴思梦), Yinlong Luo(罗寅龙), Zixin Yang(杨子鑫), Xiuyang Pang(庞修洋), Yiqiu Wang(王溢秋), Xuefen Kan(阚雪芬), Yuqiu Zhang(张雨秋), Qiang Yu(俞强), and Jian Wu(吴坚)

Citation: Chin. Phys. B, 2024, 33 (**9**): 094301. DOI: 10.1088/1674-1056/ad57ad
Journal homepage: http://cpb.iphy.ac.cn; http://iopscience.iop.org/cpb

What follows is a list of articles you may be interested in

Sensing the heavy water concentration in an H_2O—D_2O mixture by solid—solid phononic crystals

Mohammadreza Rahimi and Ali Bahrami
Chin. Phys. B, 2024, 33 (**4**): 044301. DOI: 10.1088/1674-1056/ad0bf5

Energy-distributable waterborne acoustic launcher for directional sensing

Tian Yang(杨天), Wenting Gao(高文婷), Shida Fan(范世达), Jie Ren(任捷), and Tianzhi Yang(杨天智)
Chin. Phys. B, 2023, 32 (**12**): 124302. DOI: 10.1088/1674-1056/acf5cf

Nonlinear wave propagation in acoustic metamaterials with bilinear nonlinearity

Shiqi Liang(梁诗琪), Jiehui Liu(刘杰惠), Yun Lai(赖耘), and Xiaozhou Liu(刘晓宙)
Chin. Phys. B, 2023, 32 (**4**): 044301. DOI: 10.1088/1674-1056/ac9783

Tunable topological interface states and resonance states of surface waves based on the shape memory alloy

Shao-Yong Huo(霍绍勇), Long-Chao Yao(姚龙超), Kuan-Hong Hsieh(谢冠宏), Chun-Ming Fu(符纯明), Shih-Chia Chiu(邱士嘉), Xiao-Chao Gong(龚小超), and Jian Deng(邓健)
Chin. Phys. B, 2023, 32 (**3**): 034303. DOI: 10.1088/1674-1056/ac8727

Analysis on vibration characteristics of large-size rectangular piezoelectric composite plate based on quasi-periodic phononic crystal structure

Li-Qing Hu(胡理情), Sha Wang(王莎), and Shu-Yu Lin(林书玉)
Chin. Phys. B, 2022, 31 (**5**): 054302. DOI: 10.1088/1674-1056/ac3649

Orbital angular momentum conversion of acoustic vortex beams via planar lattice coupling

Qingbang Han(韩庆邦)[1], Zhipeng Liu(刘志鹏)[1], Cheng Yin(殷澄)[1,†], Simeng Wu(吴思梦)[1], Yinlong Luo(罗寅龙)[2], Zixin Yang(杨子鑫)[2], Xiuyang Pang(庞修洋)[2], Yiqiu Wang(王溢秋)[1], Xuefen Kan(阚雪芬)[3], Yuqiu Zhang(张雨秋)[2], Qiang Yu(俞强)[2,4], and Jian Wu(吴坚)[2,‡]

[1] *College of Information Science and Engineering, Hohai University, Changzhou* 213200, *China*
[2] *College of Advanced Interdisciplinary Studies, Nanhu Laser Laboratory, National University of Defense Technology, Changsha* 410073, *China*
[3] *School of Transportation Engineering, Jiangsu Shipping College, Nantong* 226010, *China*
[4] *i-Lab, Suzhou Institute of Nano-Tech and Nano-Bionics, Chinese Academy of Sciences, Suzhou* 215123, *China*

(Received 2 April 2024; revised manuscript received 23 May 2024; accepted manuscript online 13 June 2024)

Orbital angular momentum (OAM) conversion is critical in understanding interactions between a structural sound field and a planar lattice. Herein, we explore the evolution of a monochromatic acoustic vortex beam (AVB) that is scattered by a phononic crystal (PnC) or a correlated random lattice. The phenomenon is ascribed to the enhanced orbit–orbit angular momentum coupling induced by the band structure. By modifying the coupling condition, accurate and continuous micro-manipulation of AVBs can be achieved, including the transverse/lateral gravity shift, the dynamics of the phase singularities, and the spatial distribution of acoustic pressure, etc. This research provides insight to the inhomogeneous coupling of AVBs with both propagating Bloch waves and localized Anderson modes, and may facilitate development of novel OAM-based acoustic devices for active sound field manipulation.

Keywords: acoustic vortex beam, phononic crystal, Anderson localization, Imbert–Fedorov effect

PACS: 43.40.+s, 43.20.+g, 46.40.–f, 46.40.Cd **DOI:** 10.1088/1674-1056/ad57ad

1. Introduction

Spin and orbital angular momenta (AM) are important characteristics of various waves, ranging from light wave to quantum matter wave.[1,2] Due to the analog between optics and acoustics, much effort has been devoted to generate and utilize AM-carrying acoustic beams.[3,4] Despite being curl-free, the spin AM density of inhomogeneous acoustics wave is generically nonezero,[5] which has been experimentally confirmed by observing the local particle's rotation velocity.[6] On the other hand, it is rather ubiquitous that acoustic wave also carries orbital angular momentum (OAM), which plays the key role in the wave–matter interactions.[7,8] This spiral sound, referred as acoustic vortex beam (AVB), deserves special attention for its academic importance and unique advantages over optics. Based on the rotational Doppler effect, a spatiotemporal acoustic communication system is experimentally demonstrated by transforming the multiplexed OAM channels into a temporal harmonic waveform, which can be directly demultiplexed by a single sensor configuration.[9] A reflective vortex focusing plate is applied to convert the incident waves into vortex waves, which is further applied to achieve high-speed rotation of objects. It is interesting to note that the physical scale of acoustic non-contact manipulation is greater than its optical counterpart.[10] Recent years, scholars have witnessed a rapid growth of research on the application of acoustic metasurfaces in the field of acoustic OAM, ranging from generation, modulation and detection of the AVBs.[11,12] A quasi-three-dimensional reflected metasurface is utilized to produce acoustic Bessel vortex beam with long propagation distance and broad bandwidth.[13] A continuously tunable acoustic metasurface composing of multiple layers is proposed to twist the acoustic wave and generate multiple orders AVBs.[14] Meanwhile, interactions between the conventional sound fields and various artificial structures are also drawing attention for their scientific and practical importance, especially for the potential micro-manipulation of an ultrasound beam. For instance, a generalized phased array is applied to excite and focus the ultrasonic guided waves by designing each transducer array element.[15] It has been experimentally shown that the backward shift of acoustic waves can be induced by the backward propagation in a periodical structure.[16] The eigen mode coupling between parallel clade acoustic waveguides is studied in details for its potential applications such as acoustic filters, couplers and switches.[17] Using a thin plate with periodic grating, a large shift of ultrasonic beam is realized as the energy is coupled into Lamb waves.[18] Quan *et al.* showed a way to achieve asymmetric acoustic beam splitting via the anomalous diffraction in phase gradient metasurfaces.[19]

In analogy with optics, the acoustic Goos–Hänchen (GH)

†Corresponding author. E-mail: yinch@hhu.edu.cn
‡Corresponding author. E-mail: wujian15203@163.com

© 2024 Chinese Physical Society and IOP Publishing Ltd

effect and Imbert–Fedorov (IF) effect at the interface are manifested as the lateral and transverse deviations of the spatial centroid of the scattered acoustic beams from the origin. The GH effect is due to the coherent superposition of infinite frequency components,[20] while the IF effect is intimately related to the acoustic OAM Hall effect.[21] Much effort has been devoted to enhance these effects via employing various artificial designed structures. For example, as an AVB is interacting with a metasurface, the motion of the beam centroid is related to the phase gradient of the metasurface and the incident OAM of the AVB.[22] Wang *et al.* investigated the reflection and refraction of an AVB at an ultra-thin acoustic metasurface theoretically, revealing the inner relation between the acoustic Imbert–Fedorov effect and the topological charge.[23]

In recent years, the band structure of layered metastructure or elastic metamaterials is an attractive subject.[24,25] This work focuses on the angular momentum conversion during the coupling of AVBs into various layered lattices, ranging from phononic crystal (PnC) to disordered lattice with long range correlation.[26] The PnC exhibits a succession of pass bands separated by bandgaps, whilst the random lattice induces the well-known Anderson localization.[27,28] Both structures can be effectively excited as the phase match conditions are fulfilled, resulting in successive or discrete resonant peaks in the transmission spectrum. The OAM conversion between the reflected and transmitted beams results in the transverse shifts of the AVBs, which can be significantly enhanced by efficient coupling with the structure. However, enhanced transverse shift is usually accompanied by significant distortions, since the asymmetric distribution of the twisted energy flux in a tilted reference frame results in the inhomogeneous coupling. This work provides deep insight into the coupling of acoustic OAM into artificial layered lattices, and has implications in designs of novel multi-functional acoustic vortex devices and various practical applications such as passive structural health monitoring.[29,30]

2. Scattering of an AVB by a planar lattice

Let us begin with the reflection and refraction of a paraxial Gaussian acoustic beam carrying topological charge l impinging from homogeneous medium onto the surface of a one-dimensional layered structures. As schematically illustrated in Fig. 1(a), the incident beam lies in the xOz-plane, and local coordinate frames are introduced for individual beams with each z-axis attached to the propagation directions. Due to the angular momentum conservation, the scattered beams demonstrate both lateral shift δ_x and transverse shift δ_y, which resemble their optical counterparts of the GH effect and IF effect.

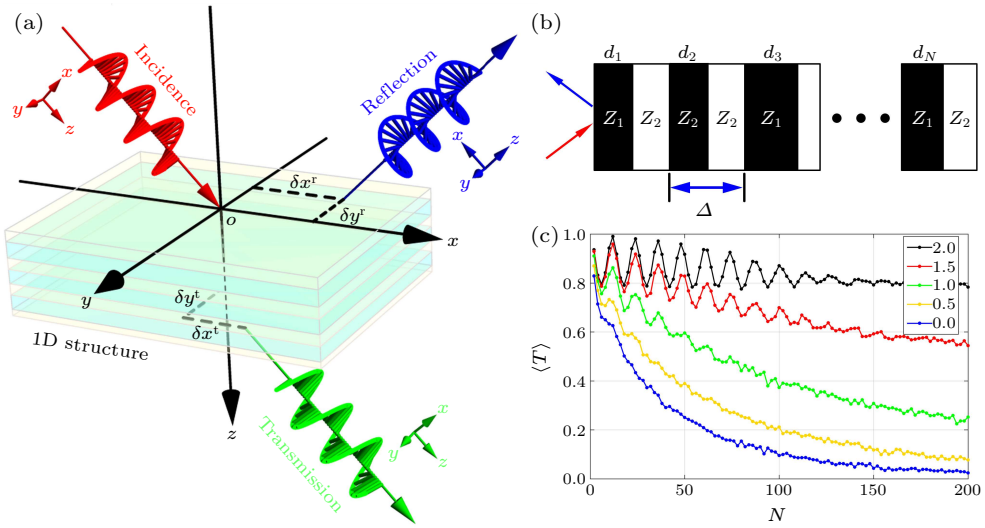


Fig. 1. Schematic diagram of the scattering of an AVB at an artificial layered lattice. (a) Reflection and refraction of an AVB at a one-dimensional planar lattice. Here δ_x and δ_y denote the transverse and lateral shifts, where the superscripts refer to the reflected and transmitted beams, respectively. The superscripts r and t refer to the reflected and transmitted beams, respectively. (b) Schematic of the one-dimensional periodic or disordered layered samples. (c) The mean transmissivity of disorder lattices corresponds to different long range correlation strength α as a function of slab number N.

The spatially varying layered lattices are generated in the form of impedance profiles by placing slabs Z_1 with variable thickness d_i in a homogeneous medium Z_2. The slabs are placed at the marked positions with fixed interval Δ for simplicity. If all the slabs have the same thickness, the system would be purely periodic, resulting in a PnC. For the random lattice, a disordered sequence consisting of N slabs with correlated random thickness d_i can be obtained using the method described in Ref. [31]. First, we create a random sequence $\eta(i)$ via generating N random numbers φ_m that are uniformly distributed in the range $[0, 2\pi]$:

$$\eta(i) = \sum_{m=1}^{N/2} \sqrt{m^{-\alpha}\left|\frac{2\pi}{N}\right|^{1-\alpha}} \cos\left(\frac{2\pi i m}{N} + \varphi_m\right). \quad (1)$$

Then the thickness of each slab is rescaled as

$$d_i = 0.96\left(1 - \frac{\eta(i)}{\eta_{\max}}\right)\Delta + 0.02\Delta, \tag{2}$$

where $\eta_{\max}$ is the maximum of the sequence $|\eta|$. The above process creates a sequence of slab thickness d_i varying between 0.02Δ and 0.98Δ. The strength of long-range correlation α determines the Anderson localization effect, which is distinct for small values of α. Generally, the sample would be less localized as the value of α increases, and become fully delocalized when α exceeds 2. Figure 1(c) depicts the transmissivity $\langle T \rangle$ averaged over 400 realizations versus N for different values of α, where the incident angle is fixed at $\theta = 0$ and the parameter α varies from 0 to 2 in steps of 0.5. For small value of α, the mean transmissivity $\langle T \rangle$ decreases exponentially with increasing lattice length, indicating that only localized states exist in these disordered lattices. For large α, the mean transmissivity mainly oscillates, since the separated Anderson modes become wider and start to merge into each other. For all the illustrations in this study, the following configuration settings are used: the interval is $\Delta = 0.02$ m, the fluid density and the sound speed of the first medium are $\rho_1 = 1000$ kg/m^3 and $c_1 = 1149$ m/s, whilst the parameters of the second medium are $\rho_2 = 1180$ kg/m^3 and $c_1 = 2175$ m/s.

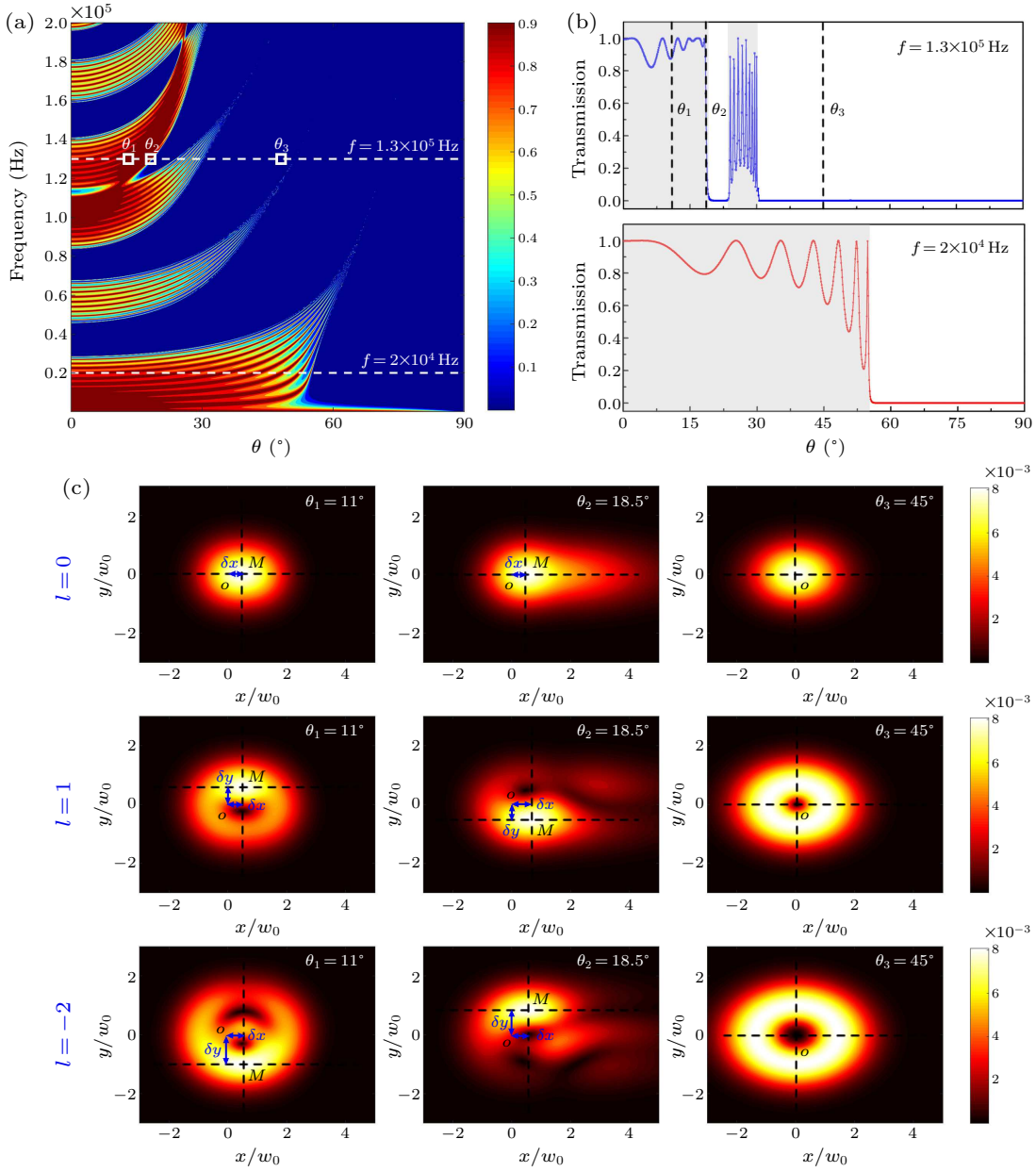


Fig. 2. The GH and IF effect of an AVB at a PnC's surface. (a) The phonon band diagram for one-dimensional PnC with slab number $N = 12$. For further usage, two selected frequencies of $f = 1.3 \times 10^5$ Hz and $f = 2 \times 10^4$ Hz are drawn by the white dashed lines, where three selected incident angles $\theta = 11°, 18.5°, 45°$ are marked by white squares. (b) The transmission through the PnC as a function of θ corresponding to the two selected frequencies. (c) The intensity pattern over the cross section of the reflected acoustic beam ($f = 1.3 \times 10^5$ Hz) at the surface of the PnC, simulated for topological charges $l = 0, 1, -2$, respectively.

3. Mode excitation and beam shifts

This study concentrates on the OAM conversion between the reflected and refracted AVBs, which induces the related GH and IF effects during the mode coupling of the planar lattices. Section A in the supplementary materials formulates the basic definitions, including the lateral shift δx^a, the transverse shift δy^a of the beam centroid $\boldsymbol{R}^a = (x_0^a\ y_0^a)^{\mathrm{T}}$ and the decomposition of the total OAM J_z^a into its intrinsic and extrinsic parts J_{int}^a, J_{ext}^a, whereas the superscripts $a = \mathrm{i}, \mathrm{r}, \mathrm{t}$ refer to the incident, reflected, and transmitted beams, respectively. For the first illustration, a PnC with only 12 slabs is considered, whose dispersion diagram exhibits discrete pass bands separated by bandgaps [Fig. 2(a)]. For comparison, the reflected pattern at the sample surface is numerically simulated for different topological charges $l = 0, 1, -2$. By varying the incident angle, the scattering of the incident AVB is considered in three different cases, i.e., the passband, the band edge, and the bandgap. For the passband ($\theta_1 = 11°$), most energy is effectively coupled into the propagating guided modes, leading to a minimum reflectivity. For the bandgap ($\theta_3 = 45°$), most energy is totally reflected, so the beam profile is less distorted and no obvious shift can be discerned in the bandgap, i.e., both GH and IF effects are trivial. For the most interesting case of the band edge ($\theta_2 = 18.5°$), the energy is partly coupled and partly reflected, accompanied by the severe distortion of the beam pattern and enhanced displacement of the beam centroid. The centroid of the incident beam is fixed at the origin o, and we compare it with the position of the maximum intensity "M" instead of the beam gravity center for a more intuitive demonstration of the beam shift. The lateral and transverse displacements of M with respect to the origin o are labeled as δx and δy and indicated by blue arrows in Fig. 1(c). At the band edge, no transverse shift can be observed for a pure Gaussian beam, while the reflected pattern is stretched along the propagation direction of the excited guided modes, resulting in a certain lateral shift δx. For the AVBs, both lateral and transverse shifts can be detected, and the direction of the transverse shift δy is determined by the sign of topological charge.[23]

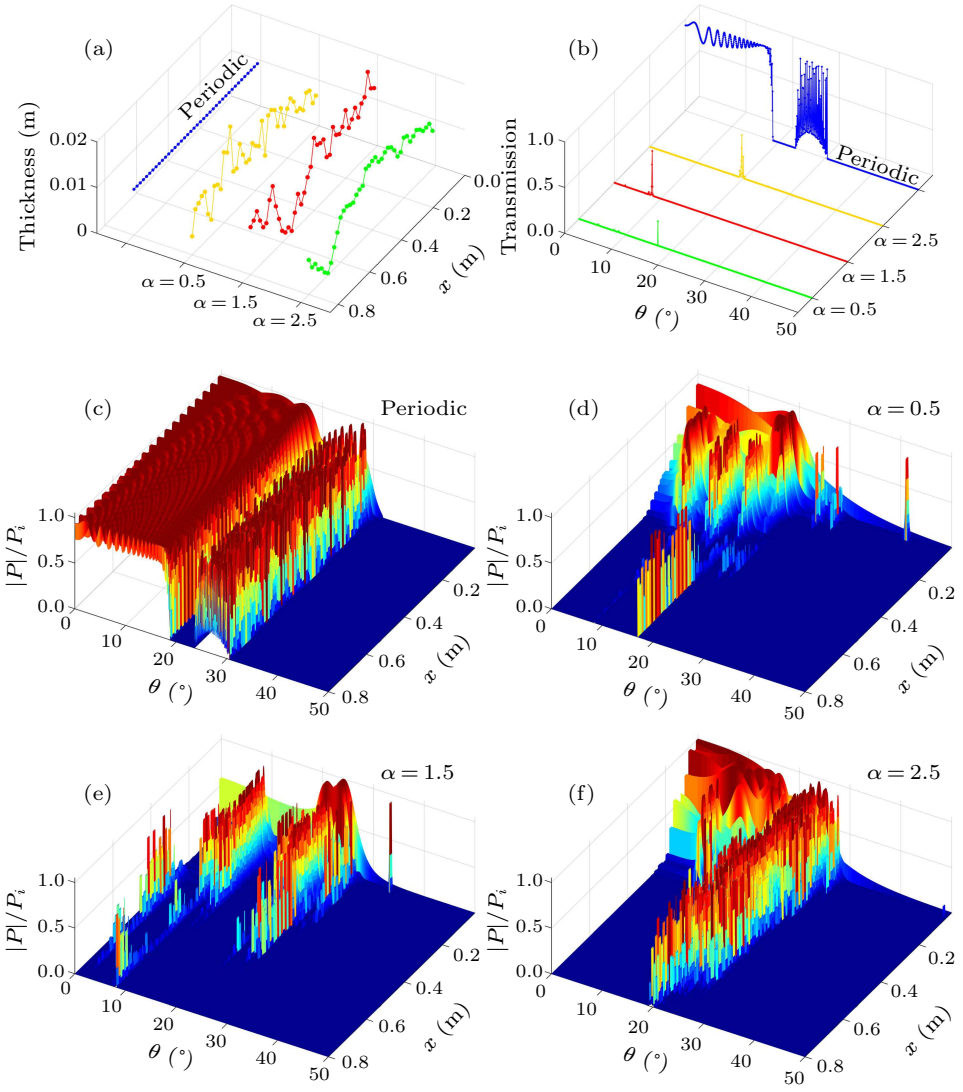


Fig. 3. The transmission and wave functions of the designed random lattice with different correlations. (a) Three realizations of random layered structures on a lattice of length $N = 40$ sites with different long-range correlations α. (b) The transmission spectra of the four realizations are simulated as a function of the incident angle with $f = 1.3 \times 10^5$ Hz. (c)–(f) The spatial distribution of the coupled acoustic mode inside the planar lattices as functions of incident angle θ and coordinate x.

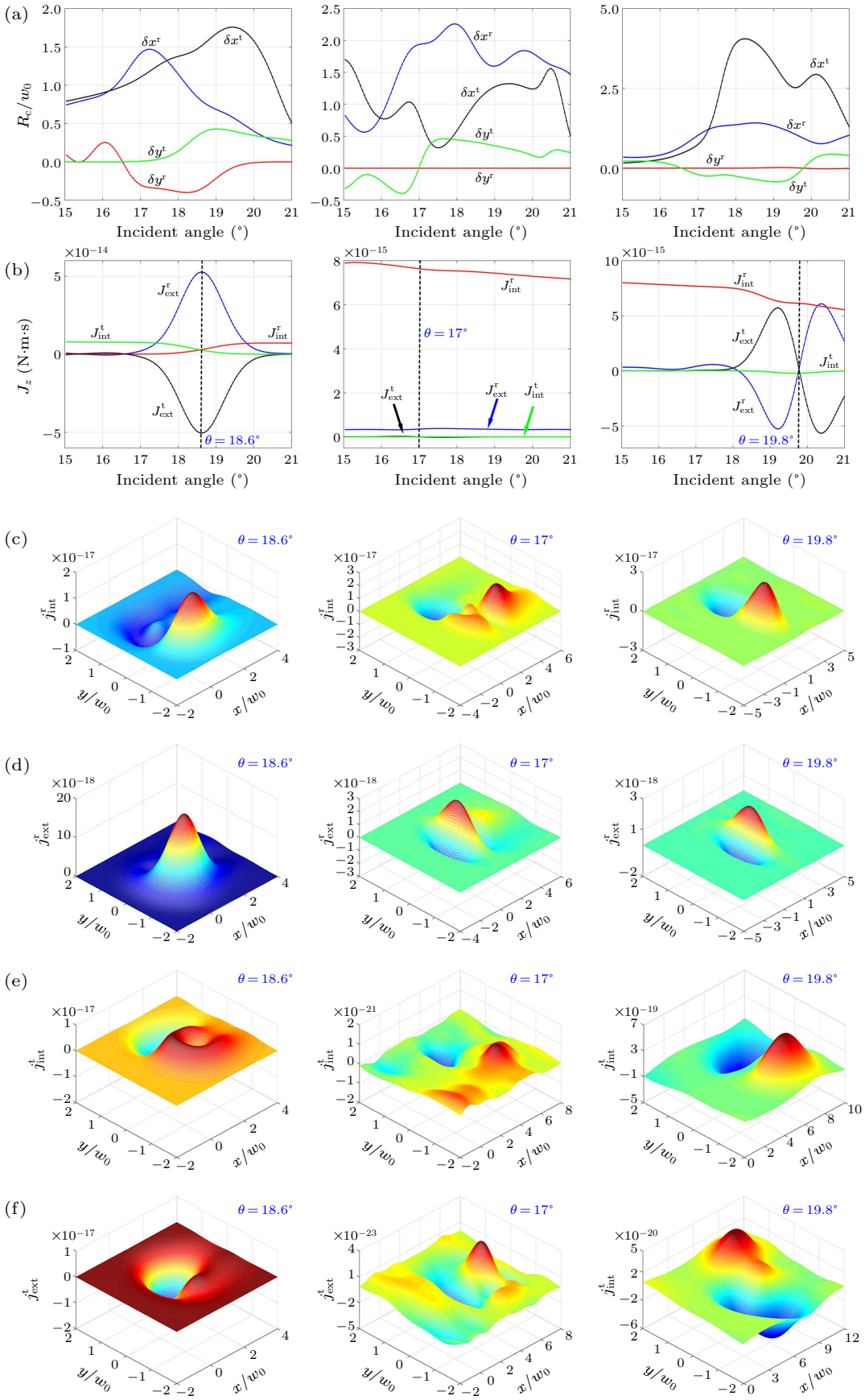


Fig. 4. The OAM conversion and the resulted centroid shifts as an AVB is incident on a PnC. (a) δx^{r}, δx^{t} and δy^{r}, δy^{t} represent the lateral and transverse displacements of the beam centroid, respectively. (b) The intrinsic and extrinsic OAM $J^{\mathrm{r}}_{\mathrm{int}}$, $J^{\mathrm{r}}_{\mathrm{ext}}$ of the reflected beam, and intrinsic and extrinsic OAM $J^{\mathrm{t}}_{\mathrm{int}}$, $J^{\mathrm{t}}_{\mathrm{ext}}$ of the transmitted beams. (c)–(f) The spatial distribution of $j^{\mathrm{r}}_{\mathrm{int}}$, $j^{\mathrm{r}}_{\mathrm{ext}}$ and $J^{\mathrm{t}}_{\mathrm{int}}$, $J^{\mathrm{t}}_{\mathrm{ext}}$ over the cross section are calculated for the selected angles. The first column corresponds to the case of periodic PnC, while the second and third columns correspond to the random arrays with $\alpha = 0.5$ and $\alpha = 2.5$, respectively. The topological charge is $l = 1$.

Notably the direction of transverse shift is reversed as the incident angle varies gradually from the pass band to the band edge, revealing the intimate relation between the IF effect and the mode coupling condition. Comparing the cases of $l = 1$ and $l = -2$, it shows that the beam profile becomes more complicated for larger value of $|l|$. Thus the IF effect of the AVBs depends on both the topological charge and the mode coupling, and the band edge brings significant distortions to the beam profile. The underlying physics can be attributed to the asymmetric coupling into the sample, which stems from the twisted flux distribution on the sample surface in a tilted frame during oblique incidence. A detailed model devoted to the asymmetric coupling is presented in Section B. The mathematics model for the scattering of the AVBs at the surface of the planar lattice can be found in Section C of the supplementary materials.

Next, the disorder is induced by randomly chosen thickness d_i of slabs Z_1, and three realizations on a lattice of length $N = 40$ with different correlated disorder are displayed in Fig. 3(a). A periodic PnC of the same length is also plotted for comparison. When the phase match condition of the layered structure is fulfilled, the incident energy may be coupled into the guided or localized mode, resulting in a resonant peak in the transmission spectrum. Transfer matrix method is applied to calculate the transmissivity for all the samples in Fig. 3(b); and the corresponding wave functions inside the structures are depicted in Fig. 3(c). The simulation shows that the state in the pass band of the PnC extends over the whole samples, leading to high transmission probability in the pass band. In contrast, the states in the disordered systems are localized in space, resulting in nearly zero transmission for most incident angles.

However, the transmission could be very close to unit for some specific incident angles, which manifest as discrete sharp peaks in the transmission spectrum. These situations are extremely sensitive to small variations of the structural arrangement, and a slight change to the lattice configuration would remove the peak completely. We are particularly interested in such cases, which allow us to investigate the orbit-orbit coupling between the reflected and transmitted beams via the excitation of localized modes. To be utilized later, two cases of near unit transmission in Fig. 3 are selected with $\theta = 17^\circ$ for $\alpha = 0.5$, and $\theta = 19.8^\circ$ for $\alpha = 2.5$, respectively. The long-range correlation determines the full width half maximum (FWHM) of the resonant peaks, where small α usually corresponds to small FWHM, and the related wave function becomes more tightly localized in space. It would be clear later that the OAM conversion is significantly enhanced at these abrupt variations in the transmission spectra, like the band edge of the PnC and the resonant peaks of the disordered lattices.

4. The OAM conversion

Scattered by the layered sample, the orbit–orbit coupling of the angular momentum transforms between the reflection and transmission. Take the mode leakage into consideration, the reflected beam is generated via the interference of two parts: the direct reflection at the sample surface and the leakage of the coupled modes. In contrast, the transmitted beam originates only from the mode leakage from the bottom. In Fig. 4, we depict the lateral and transverse shifts, the intrinsic and extrinsic OAMs for the three examples designed in Section 3 of the supplementary materials, including the PnC, the two disordered systems with $\alpha = 0.5$ and $\alpha = 2.5$. The topological charge is $l = 1$, while the case of $l = -2$ is presented in Section C of the supplementary materials. All the centroid shifts are calculated and normalized to the beam waist. In view of Fig. 4(b), it is obvious that mutual conversion exists between the $J^{\mathrm{r}}_{\mathrm{ext}}$ and $J^{\mathrm{t}}_{\mathrm{ext}}$, and the underlying physics can be attributed to the asymmetric coupling effect induced by oblique incidence. The spatial distribution of localized incident angle θ_{L} (defined in Section B of the supplementary materials) is asymmetric along the y-axis. Thus the centroids of the reflected and transmitted beams are transversely shifted, which gains insight into the acoustic Imbert–Fedorov effect.

Consider the details of the mutual conversion between the extrinsic OAMs of the reflection and transmission channels, the simulated OAM conversion of the PnC is one order larger than the disordered sample with $\alpha = 2.5$, and two orders larger than the disordered structure with $\alpha = 2.5$. For the reflected beams, the transverse shifts for the disordered lattices are much smaller than that of the PnC; whereas the transverse shifts of the transmitted beams are of the same order for all the examples. This can be well understood by considering the low transmission probability of random lattices, since only a small portion of the twisted wave front possesses the required wave vector to excite the localized mode. For the disordered lattice, the transverse shift of the reflected beam is small since most reflected energy has not participate the OAM conversion. In contrast, the transmitted beam induced by the mode leakage is fully influenced by the orbit–orbit coupling, guaranteeing a large transverse shift. At the band edge of a PnC, the transverse shifts of both reflected and transmitted beams are significant, since a large portion of energy participates the orbit–orbit coupling.

Another key factor underlying the conversion mechanism is its connection with the structure of the transmission spectrum, which is simulated in Fig. 4. For the PnC, there exists a step-like structure in the transmission spectrum at the band edge. In the region of pass band of the PnC, only refracted beam carries intrinsic OAM, and no beam carries extrinsic OAM. As the incident angle approaches the band edge, the

reflected beam gains positive extrinsic OAM, while the transmitted gains negative extrinsic OAM. The extrinsic OAM conversion reaches its maximum at $\theta = 18.6°$, which matches well with the position of the band edge. As the incident angle further increases, the extrinsic OAM conversion decreases gradually to zero. Meanwhile, the intrinsic OAM is totally transferred from the transmitted beam to the reflected beam after passing the band edge. The above described process can be denoted as a OAM conversion at the falling edge of the transmission spectrum. Similarly, the sharp resonant peak of the disordered lattice can be treated as a combination of two abrupt steps, i.e., a rising edge and a falling edge. Thus there exist two OAM conversion processes around the resonant peak, while the middle position $\theta = 19.8°$ coincides with the resonant peak. The above statements can serve as a strong evidence that the mode coupling process significantly boosts the OAM conversion. The positions of the band edge and the resonant peaks are marked out as vertical dashed lines, and the distributions of the intrinsic and extrinsic OAM density correspond to these critical angles are also simulated in Fig. 4(c). The case of topological charge $l = -2$ can be found in Section D of the supplementary materials. To sum up, during the interaction with the layered lattice, the gravity center of the reflected and refracted beams shift due to the OAM conversion, which is significantly enhanced as the transmission varies abruptly. These findings may be helpful for manipulation of beam shifts via adjusting mode coupling condition of the layered lattices.

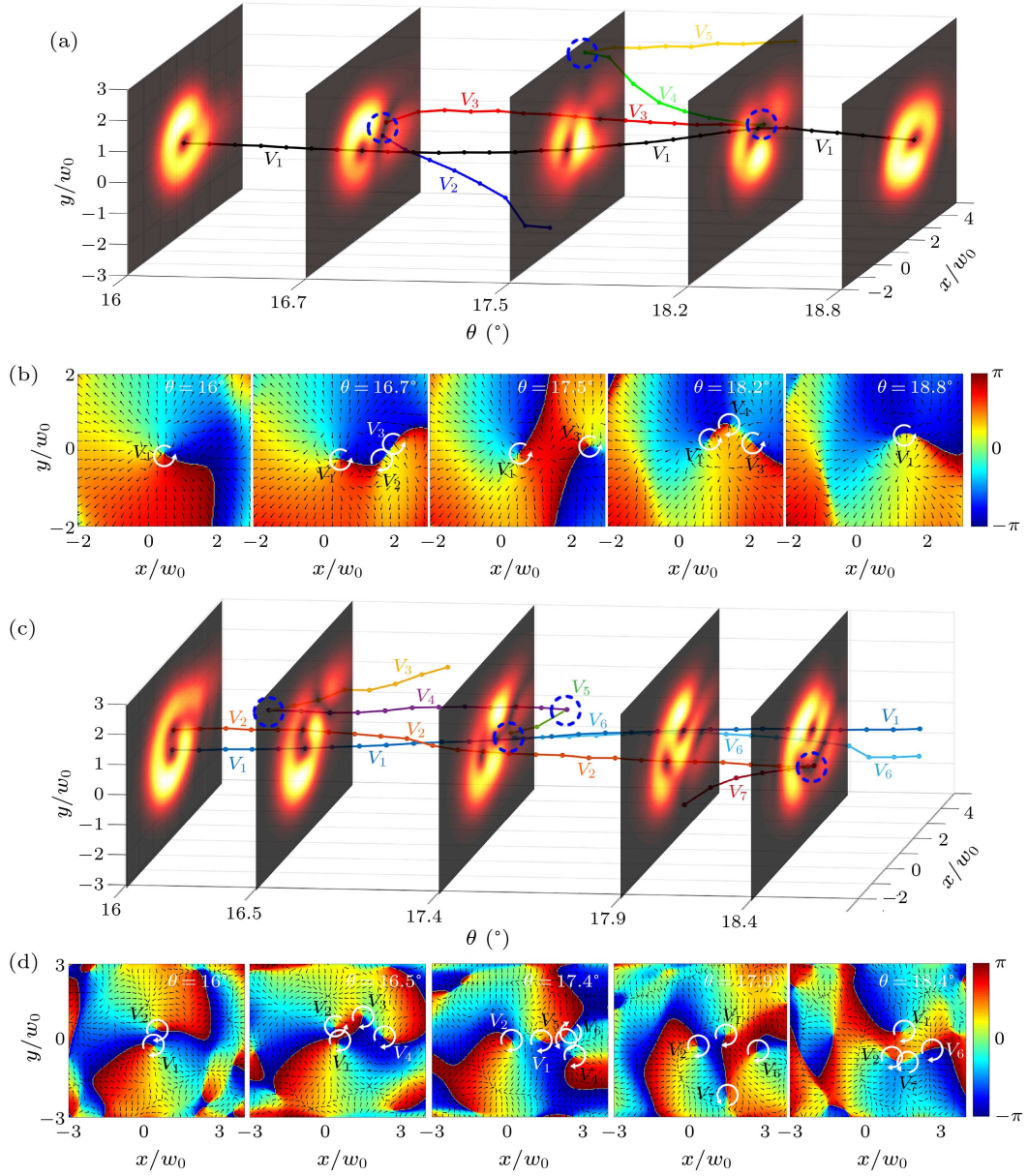


Fig. 5. Topological events on the cross section during the evolution of a reflected AVB by varying the incident angles. (a) The evolution of the beam patterns and the trajectories of the vortex cores (lines) as an AVB ($l = 1$) is reflected at the surface of the PnC. (b) The phase profiles in the cross sections, where the small black arrows indicate the distribution of the transverse linear momentum. The white circles indicate the vortex core with $l = \pm 1$, respectively. (c) and (d) Similar to (a) and (b) except that the topological charge of the incident AVB is $l = -2$.

5. Vortices dynamics

Similar to the singular optics, the instantaneous pattern of the AVB is organized by its singular "skeleton", which consists of various singularities, such as vortex, saddle and extrema. Therefore, the evolution of the scattered AVBs in the coupling of the planar lattices can also be investigated from different perspectives of topological events of these singularities. In this context, the dynamics of vortices in the cross section of the beam plays the key role, such as generation, splitting, collision, annihilation, and drift. Apparently, the severe distortions of the reflected beam is due to the sophisticated dynamics of the vortex cores with null-pressure center. Figure 5 shows the simulated results for the PnC with topological charge $l = 1, -2$, and the related results for the two random samples can be found in Section E of the supplementary materials. The generation and annihilation of the vortex pairs with opposite handedness are marked with blue dashed circles, whilst the beam patterns and the corresponding phase profiles are simulated at certain propagation distances. As the incident angle increases continuously around the band edge, the reflected beam can gain or loss vortices from void. In contrast, the transmitted beam is less distorted, since it carries only one vortex for all the incident angles. Similarly, the underlying physics can be attributed to their formation mechanisms: the reflected beam originates from the interference, while the transmitted beam results from the mode leakage alone. Thus, vortices are produced or annihilated in pairs in the reflected beam, obeying the angular momentum conservation. The dynamics of the vortices can be predicted by considering the transverse flux distribution over the cross section, which demonstrates the particle-like nature. Finally, the above-described dynamics also relies crucially on the abrupt variation of the transmission, which opens up the exchange channel of the OAM between the reflection and refraction. In Section F of the supplementary materials, we compare the scattering of AVBs with higher order topological charges. In Section G of the supplementary materials, the transmission issue is discussed in detail.

6. Conclusion

In conclusion, the OAM is converted between the reflected and transmitted beams as an AVB interacting with an artificial layered structure, resulting the acoustic IF effect. The acoustic GH effect is due to the mode coupling and independent of the acoustic OAM. The extrinsic OAM is generated due to the asymmetric coupling of the sample in a tilted frame, and the conversion can be adjusted by the mode excitation condition. By coupling with the guided modes in PnC or localized modes in random lattices, it shows that the OAM conversion can be effectively enhanced at abrupt transmission variations, accompanied by large transverse shift. By actively adjusting the mode coupling condition of the artificial layered lattices, our scheme provides a methodology for micro-manipulation of the AVBs with high precision.

Acknowledgments

This work was supported by the National Natural Science foundation of China (Grant No. 12174085), the Fundamental Research Funds for the Central Universities (Grant No. B220202018), the Basic Science (Natural Science) Research Project for the Universities of Jiangsu Province (Grant No. 23KJD140002), and Natural Science Foundation of Nantong (Grant No. JC2023081).

References

[1] Li L, Guo Y, Zhang Z, Shang Z, Li C, Wang J, Gao L, Hai L, Gao C and Fu S 2023 *Adv. Photon.* **5** 056002
[2] Mondal PK, Deb B and Majumder S 2015 *Phys. Rev.* **92** 043603
[3] Li X R, Jia Y R, Luo Y C, Yao J and Wu D J 2021 *Appl. Phys. Lett.* **118** 043503
[4] Gao S, Li Y, Ma C, Cheng Y and Liu X 2021 *Nat. Commun.* **12** 2006
[5] Bliokh K Y and Nori F 2019 *Natl. Sci. Rev.* **99** 174310
[6] Shi C, Zhao R, Long Y, Yang S, Wang Y, Chen H, Ren J and Zhang X 2019 *Natl. Sci. Rev.* **6** 707
[7] Zou Z, Lirette R and Zhang L 2020 *Phys. Rev. Lett.* **125** 074301
[8] Fan S W, Wang Y F, Cao L, Zhu Y, Chen A L, Vincent B, Assouar B and Wang Y S 2020 *Appl. Phys. Lett.* **116** 163504
[9] Zhang C, Jiang X, He J, Li Y and Ta D 2023 *Adv. Sci.* **10** 2206619
[10] Ruan Y, Zhu J, Lin Q, Wang Y, Zhou D, Wang S, Li C, Shi J and Chen R 2024 *J. Sound Vibr.* **581** 118380
[11] Fu Y, Tian Y, Li X, Yang S, Liu Y, Xu Y and Lu M 2022 *Phys. Rev. Lett.* **128** 104501
[12] Jiang X, Li Y, Liang B, Cheng J and Zhang L 2016 *Phys. Rev. Lett.* **117** 034301
[13] Wang Y and Qian J 2021 *Micromachines* **12** 1388
[14] Gong K, Zhou X and Mo J 2022 *Smart Mater. Struct.* **31** 115001
[15] Zhang B, Dong H and Gong J 2013 *Acoust. Phys.* **59** 97
[16] Xu Z, Qian M L, Cheng Q and Liu X J 2016 *Chin. Phys. Lett.* **33** 114302
[17] Yin G, Li P, Yang X, Tian Y, Han J, Ren W and Guo J 2022 *Acta Acust.* **6** 101051
[18] Li D, Yan X, Xu Z and Ta D 2019 *Ultrasonics* **95** 32
[19] Quan J, Sun B, Fu Y, Gao L and Xu Y 2024 *Chin. Phys. Lett.* **41** 014301
[20] Fa L, Xue L, Fa Y, Han Y, Zhang Y, Cheng H, Ding P, Li G, Tang S, Bai C, Xi B, Zhang X and Zhao M 2017 *Sci. China Phys. Mech. Astron.* **60** 104311
[21] Fan X and Zhang L 2021 *Phys. Rev. Res.* **3** 013251
[22] Wang W, Liu J, Liang B and Cheng J 2022 *Chin. Phys. B* **31** 094302
[23] Wang W, Tan Y, Liang B, Ma G, Wang S and Cheng J 2021 *Phys. Rev. B* **104** 174301
[24] Bastawrous M V and Hussein M I 2021 *J. Sound Vibr.* **514** 116428
[25] Jin Y, Jia XY, Wu Q Q, He X, Yu G C and Wu L Z 2022 *J. Sound Vibr.* **521** 116721
[26] Overy A R, Simonov A, Chater P A, Tucker M G and Goodwin A L 2017 *Basic Solid State Phys.* **254** 1600586
[27] Hu H, Strybulevych A, Page J H, Skipetrov S E and van Tiggelen B A 2008 *Nat. Phys.* **4** 945
[28] Hu R and Tian Z 2021 *Phys. Rev. B* **103** 045304
[29] Wang J, Huo L, Liu C and Song G 2021 *Struct. Health Monit.* **20** 2917
[30] Gao W, Zhang C, Song G and Li H N 2021 *Struct. Health Monit.* **20** 188201
[31] De Moura F A and Lyra M L 1998 *Phys. Rev. Lett.* **81** 3735